RSC Advances

PAPER

View Article Online
View Journal | View Issue

Cite this: *RSC Adv.*, 2024, **14**, 2687

Exploring the effect of boron on the grain morphology change and spectral properties of Eu^{3+} activated barium tantalate phosphor

Mustafa İlhan, *[a] Lütfiye Feray Güleryüz [b] and Mehmet İsmail Katı[c]

The effect of the grain morphology on the photoluminescence, charge transfer band, and decay properties was investigated by xEu^{3+}, yB^{3+} (x = 10 mol%, y = 0, 5, 15, 30, 50, 70, and 100 mol%) co-doped $BaTa_2O_6$ ceramics fabricated by solid-state reaction. X-ray diffractions of the samples showed that the single-phase structure persisted up to 100 mol% and there was an improvement in crystallinity with increasing B^{3+} concentration. SEM micrographs of the Eu^{3+}, B^{3+} co-doped grains showed that the flux effect of boron promotes grain growth and elongated grain shape. The PL emissions of the $BaTa_2O_6$:xEu^{3+}, yB^{3+} co-doped phosphors increased up to 100 mol% B^{3+} concentration, and there was an increase in the intensities of the CTB energy $^5D_0 \rightarrow {}^7F_1$ transition. The increase in PL may be attributed to the increased grain size leading to a decrease in the surface area (SA)/volume (vol) ratio with increasing B^{3+} concentration, as well as the improvement in crystallinity. However, the decrease in asymmetry ratio was related to the occupation of centrosymmetric (B) sites and the transformation from a rounded/irregular-like to an elongated/rod-like grain shape which has an increasing effect on the SA/vol ratio. The decreasing trend of the Judd–Ofelt parameters (Ω_2, and Ω_4) with the increase in boron was related to a high local symmetry of Eu^{3+} sites, and an increase in the electron density of the surrounding ligands, respectively. The increase in boron led to longer decays in the observed lifetime with bi-exponential characteristics. The CIE diagram and UV lamp photographs of the phosphors showed a color transition from red to orange associated with the increasing magnetic dipole transition. This study may provide an alternative perspective and new strategies to describe the control of grain morphology and luminescence concerning RE-doped phosphors.

Received 30th November 2023
Accepted 9th January 2024

DOI: 10.1039/d3ra08197d

rsc.li/rsc-advances

1. Introduction

Promising advances are being made in a variety of applications, including solid-state lasers, LEDs, optical communication, and temperature sensing, due to the activation of phosphors with trivalent rare earth ions (RE^{3+}). Their unique optical properties such as extended luminescence times, narrow emission ranges, and excellent photostability are of great interest.[1–8] In the development of luminescent materials, the grain morphology of ceramic phosphors has an effect on the luminescence. Therefore, the grain size, and grain shape of phosphor may play an important role in the correlation between the material and spectral properties.[9–19] In the literature, researchers have drawn attention to the effects of morphological features such as grain size and grain shape on the luminescence mechanism, where the surface area (SA) to volume (vol) ratio is an important parameter.[9–19] Boron vitrification plays an effective role in grain morphology, increasing crystallization, reducing sintering temperature, and improving optical and structural properties.[18–22] The enhancement of luminescence with boron doping has been pointed out in many studies to be related to improved crystallinity.[23–25] However, there are also some studies showing the luminescence increase along with the decrease in crystallization with the doping of boron.[26,27] The photoluminescence of boron co-doped $Ba_{0.88}Mg_{0.93}Al_{10}O_{16.96}$:$Eu^{3+}$ phosphor has been studied by Dulda *et al.*[28] where the grain size and crystallinity of phosphor increased as the grain shape changed from rod to hexagonal shape. Moreover, some studies have been performed by İlhan *et al.* on Eu^{3+}, B^{3+} co-doped $SrTa_2O_6$,[18] and Dy^{3+}, B^{3+} co-doped $CdNb_2O_6$ (ref. 19) phosphors, where it is emphasized that the increased luminescence is closely related to grain morphology.

Tetragonal is the middle-temperature polymorph of $BaTa_2O_6$ that occurs between 1150–1300 °C, and this polymorph related to tetragonal tungsten bronze (TTB) structure which can remain kinetically stable at high temperatures (*e.g.* 1550 °C).[29–31] TTB crystal structure belongs to a wide family of functional materials

[a]*Department of Environmental Engineering, Faculty of Engineering, Marmara University, Maltepe, 34854, İstanbul, Turkey. E-mail: mustafa.ilhan@marmara.edu.tr*
[b]*Department of Tobacco Technology Engineering, Manisa Celal Bayar University, Akhisar 45200, Manisa, Turkey*
[c]*Department of Medical Imaging Techniques, Vocational School of Health Sciences, Manisa Celal Bayar University, 45030, Manisa, Turkey*

and offers a large scale of doping possibilities due to its suitable structure for different cationic dopants. TTB oxide structures having the $A_2BC_2M_5O_{15}$ formula (M = Ta, Nb) consist of three types of sites in which the pentagonal (A), square (B), and triangular (C) tunnels are represented by 15, 12, and 9 CN, respectively.[29,30]

In this paper, we reported the effect of grain size and grain shape on spectral properties with a systematic study, which has been scarcely researched before in the literature. In our previous two studies,[18,19] effect of boron dopant has been examined up to 20 and 25 mol% concentrations, respectively. However, in this detailed study, the relationship between spectral properties and grain morphology was investigated by increasing the boron concentration up to 100 mol%, and interesting results were obtained. Depending on the structural and morphological changes with increasing boron concentration, the effects of varying grain size, grain shape, and different SA/vol ratios on luminescence, charge transfer band, decay properties, and Judd–Ofelt parameters were studied by applying XRD, SEM, PL, and decay analyses.

2. Experimental

$BaTa_2O_6$:xEu^{3+}, yB^{3+} (x = 10 mol%, y = 0, 5, 15, 30, 50, 70, 100 mol%) samples were fabricated by solid-state method. The $BaCO_3$ (Sigma-Aldrich, 99%), Ta_2O_5 (Alfa Aesar, 99.9%), Eu_2O_3 (Alfa Aesar, 99.9%), and H_3BO_3 (Kimyalab, %99.9) were used in the synthesis process. The stoichiometric amount of the starting materials was mixed and ground well in an agate mortar to provide homogeneity. Then, by adding europium oxide (Eu_2O_3) and boric acid (H_3BO_3), the final mixture of the powders was thoroughly mixed and ground in an agate mortar for the last time to provide more homogeneity. For the sintering process, a sufficient amount of mixture was taken and sintered in an alumina crucible at 1425 °C for 20 h after pelleting.

The phase compositions of the samples were identified by XRD (X-ray diffractometer; PANanalytical Empyrean, U.K.) using Cu Kα radiation between 2θ = 20–70 °C with scan speed 2 ° C min^{-1}. The grain morphologies of the samples were investigated by SEM (scanning electron microscopy; FE-SEM; Gemini 500, Zeiss Corp., Germany). Photoluminescence (PL) results were taken by a fluorescence spectrometer (FLS920, Edinburgh Instruments, UK) equipped with a 450 W ozone-free Xe lamp. Lifetime data were also obtained by a fluorescence spectrometer (FLS920) using the time-correlated single-photon counting (TCSPC) system. All the analyses were performed at room temperature.

3. Results and discussions

3.1 XRD and SEM results

XRD results of 10 mol% Eu^{3+} and yB^{3+} (y = 0, 5, 15, 30, 50, 70, 100 mol%) co-doped $BaTa_2O_6$ ceramic samples are shown in Fig. 1. XRD patterns of $BaTa_2O_6$ showed a single tetragonal tungsten bronze structure (JCPDS card no: 17-0793) with space group $P4/mbm$ (127). The absence of any minor phase can be explained by the successful incorporation of Eu^{3+} ions in the A and B sites of the TTB host and the dissolution of co-doped boron with different concentrations in the three tunnels of the structure. On the other hand, increasing B^{3+} concentration led to an increase in (001) and (002) XRD reflections, which would be attributed to a z-direction orientation. As mentioned in the SEM part, this phenomenon is related to the grain elongation of $BaTa_2O_6$ at high temperatures,[31,32] and also the boron vitrification may cause a similar effect in the structure. The shift of XRD peaks (311) towards the smaller two theta angles is shown in Fig. 2. The B^{3+} ions occupying the structure with a small ionic radius potentially caused an expansion in the lattice due to increased positive charge. Table 1 summarizes the variation of lattice data of all samples. The lattice data for 0 and 100 mol% B^{3+} samples are a = 12.6272 Å, c = 3.8916 Å, V = 620.51 $Å^3$, and a = 12.7436 Å, c = 3.9052 Å, V = 634.20 $Å^3$, respectively, in which the lattice volume increased as 2.2%. Additionally, in Fig. 2, the narrowing XRD peaks with increasing B^{3+} indicate an increase in crystallinity. The crystallite size of the samples determined using the Scherrer equation is given in Table 1, where the crystallite sizes from 0 to 100 mol% B^{3+} co-doped samples changed to 32.58 and 50.53 nm, respectively. The enhancement in crystal size may be attributed to the reduction in nucleation and lattice deformation resulting from increased boron concentration.

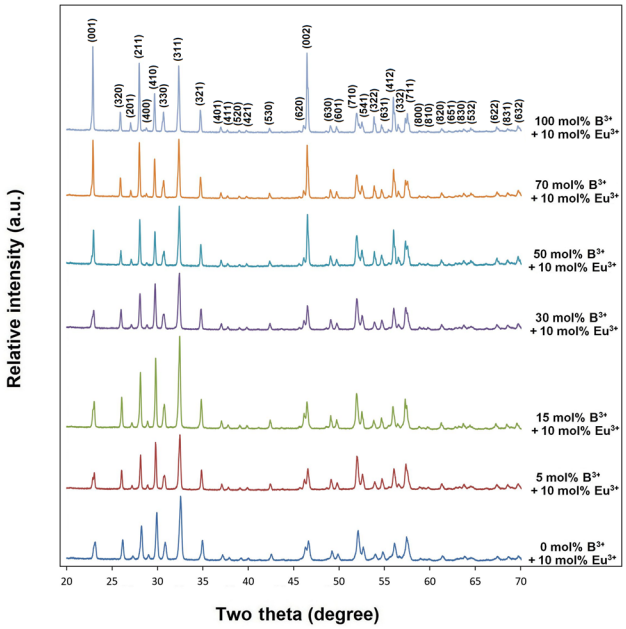

Fig. 1 XRD results of 10 mol% Eu^{3+} and 0, 5, 15, 30, 50, 70, and 100 mol% B^{3+} co-doped $BaTa_2O_6$ samples.

Fig. 3(a–g) shows SEM micrographs of Eu^{3+}, B^{3+} co-doped ceramic samples at 5000× magnification and 10 kV acceleration voltage. As seen from the SEM micrographs, boron doping promoted agglomeration, grain growth, and rod-like shape in grains. The elongation tendency of grains may be attributed to the vitrification effect improved by the presence of B^{3+}, which is supported by (001) and (002) XRD reflections. In Fig. 3a, the undoped boron sample has a small grain size, and a round-like

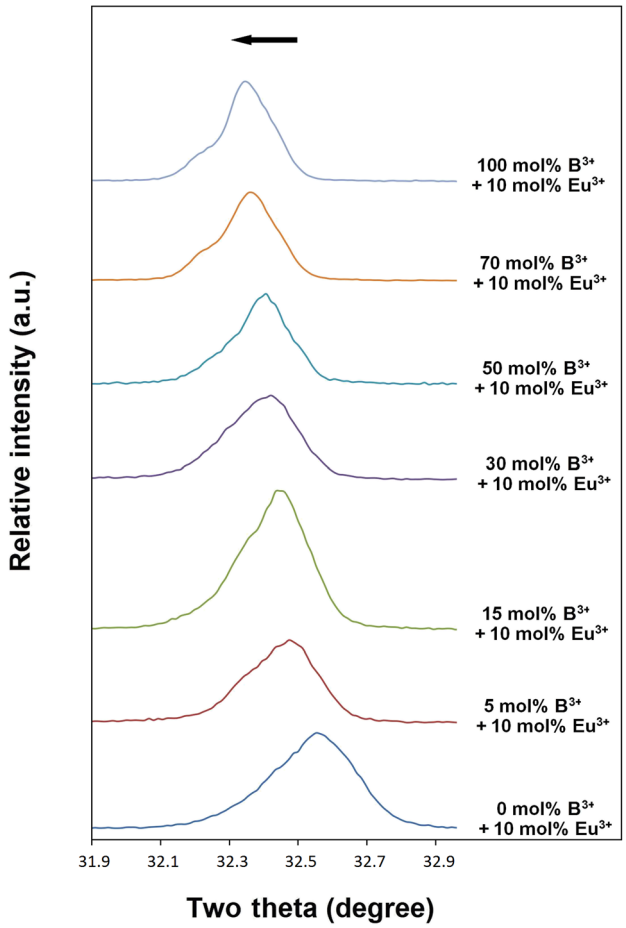

Fig. 2 Shift of XRD two theta peaks (311) to lower angles.

Table 1 Cell parameters and average crystallite sizes for Eu^{3+}, B^{3+} co-doped $BaTa_2O_6$

Sample	Lattice parameters			Crystallite size
	a (Å)	c (Å)	V (Å)^3	D (nm)
JPCDS card no. 17-0793	12.5600	3.9580	624.39	—
0 mol B^{3+} 10 mol% Eu^{3+}	12.6272	3.8916	620.51	32.58
5 mol B^{3+} 10 mol% Eu^{3+}	12.6452	3.8986	623.39	39.60
15 mol B^{3+} 10 mol% Eu^{3+}	12.6740	3.8990	626.30	41.68
30 mol B^{3+} 10 mol% Eu^{3+}	12.7024	3.9004	629.33	40.48
50 mol B^{3+} 10 mol% Eu^{3+}	12.7088	3.9010	630.07	48.49
70 mol B^{3+} 10 mol% Eu^{3+}	12.7364	3.9046	633.39	49.71
100 mol B^{3+} 10 mol% Eu^{3+}	12.7436	3.9052	634.20	50.53

irregular grain-shaped morphology, while the grain sizes usually range from 0.5 to 1.5 μm. In Fig. 3b, the growing and elongating tendency of the grains started to occur in the 5 mol% B^{3+} co-doped sample, and it became more pronounced at 15 mol% B^{3+} (Fig. 3c). In Fig. 3d, the grain shape of 30 mol% B^{3+} doped sample had almost rod-like and thick-grained appearance while the growth and elongation trend in the grains continued for higher B^{3+} concentrations as seen in Fig. 3(e–g). In Fig. 3e, the amount of the grains with small size was considerably decreased at 50 mol% B^{3+}, and it nearly disappeared at 70 (Fig. 3f) and 100 mol% (Fig. 3g) B^{3+} concentrations. The grain sizes for the without boron sample varied between 0.5–3.0 μm, while the thicknesses and lengths of the grains reached the range of 1.5–10 μm and 5–40 μm, for 100 mol% B^{3+} concentration, respectively.

3.2 Spectral properties for $BaTa_2O_6$:$x$$Eu^{3+}$, $y$$B^{3+}$ (x = 10 mol%, y = 0, 5, 15, 30, 50, 70, and 100 mol%) phosphors

Fig. 4 shows PL excitation spectra of $BaTa_2O_6$:$x$$Eu^{3+}$, $y$$B^{3+}$ (x = 10 mol%, y = 0, 5, 15, 30, 50, 70, 100 mol%) phosphors recorded at λ_{em} = 618 nm. PL excitations of all the phosphors were assigned by the $^7F_0 \rightarrow {}^5D_4$, $^7F_0 \rightarrow {}^5G_J$, $^7F_0 \rightarrow {}^5L_6$, $^7F_0 \rightarrow {}^5D_3$, and $^7F_0 \rightarrow {}^5D_2$ transitions, which are related to the intra-configurational (f–f) transitions of Eu^{3+}. In Fig. 4, the peaks associated with the CTB transition have a broadband and a maximum in the 340–350 nm range. The CTB peaks over 300 nm are related to the ligand nature of TTB structure due to the ligand environment with highly coordinated A and B tunnels.[33,34] As reported in similar studies,[18,29] the CTB transition intensity increased with increasing intensity of magnetic dipole transition or the formal reduction of Eu^{3+} to Eu^{2+} is increasing. Fig. 5 shows the PL emissions of $BaTa_2O_6$:$x$$Eu^{3+}$, $y$$B^{3+}$ (x = 10 mol%, y = 0, 5, 15, 30, 50, 70, 100 mol%) phosphors monitored by the $^5D_0 \rightarrow {}^7F_J$, ($J$ = 0, 1, 2, 3, 4, 5) transitions under excitation of 394 nm, in which the phosphor luminescence increased up to 100 mol% B^{3+} concentration. The increase in luminescence can be evaluated in terms of crystallinity and morphology. As mentioned in XRD results, the improved crystallinity will contribute to the increase of the luminescence of $BaTa_2O_6$:Eu^{3+}, B^{3+}. On the other hand, literature results on the luminescence increase despite decreasing crystallinity[26,27] show that morphological parameters such as grain size and grain shape are very important in the increase in luminescence. The effects of the grain size and grain shape on luminescence are reported by different researchers. Kim and Kang[9] highlighted that an increase in grain size led to an increase in luminescence due to the reduced presence of non-luminescent centers near the grain surface. Shan *et al.*[10] investigated the effects of nanocrystals with different shapes on luminescence using surface area (SA)/volume (vol) ratios. Some researchers[11–13] suggested that phosphors with spherical grain morphology exhibit superior spectral characteristics, including reduced light scattering, enhanced luminescence, and higher definition. Accordingly, the effect of boron may be evaluated in terms of size and shape changes in the grains. Although the increase in boron concentration caused the grain size to increase, there was a deviation from the spherical grain shape due to grain elongation. The transformation of the grains from an irregular/round-like shape to an elongated/rod-like shape would be likely to support an increase in the SA/vol ratio. However, if the grain shape is preserved or there is no grain elongation, grain growth will contribute more to the decrease of the SA/vol ratio, and the activation of luminescence centers near the surface will increase further. In this process, since grain

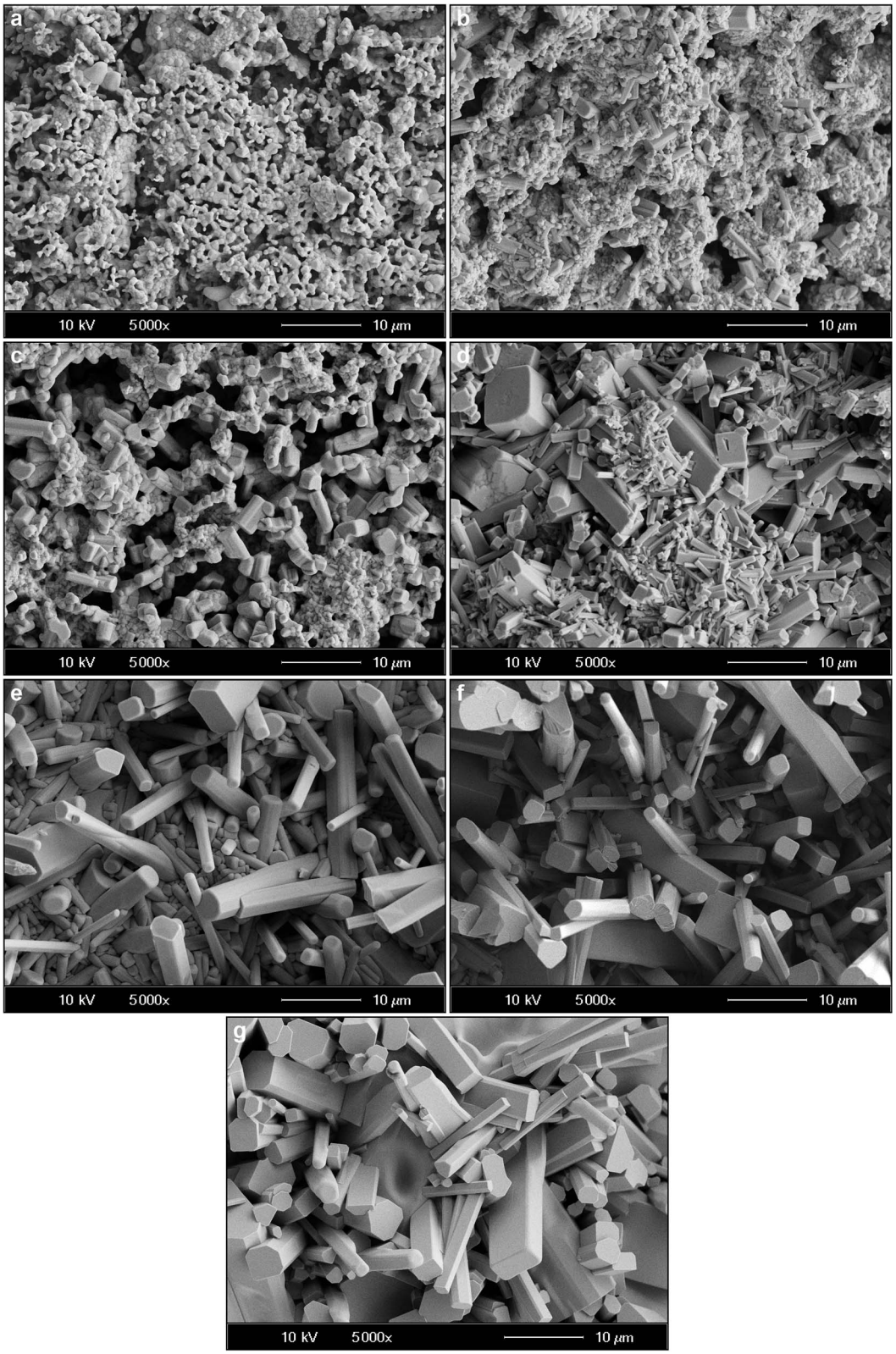

Fig. 3 SEM micrographs of 10 mol% Eu^{3+}, and different concentrations B^{3+} co-doped $BaTa_2O_6$ samples: (a) 0 mol%, (b) 5 mol% B^{3+}, (c) 15 mol% B^{3+}, (d) 30 mol% B^{3+}, (e) 50 mol% B^{3+}, (f) 70 mol% B^{3+}, (g) 100 mol% B^{3+}, under 10 kV accelerating voltage at 5.000× magnifications.

growth and grain elongation occur together, grain elongation will contribute to an increase in the SA/vol ratio. However, although there is an increase in luminescence, the difference in asymmetry ratio ($^5D_0 \rightarrow {}^7F_2/{}^5D_0 \rightarrow {}^7F_1$) is remarkable. The variation of the asymmetry ratio and B^{3+} concentration is shown in Fig. 6. The emission increases were about 11 and 3 fold from

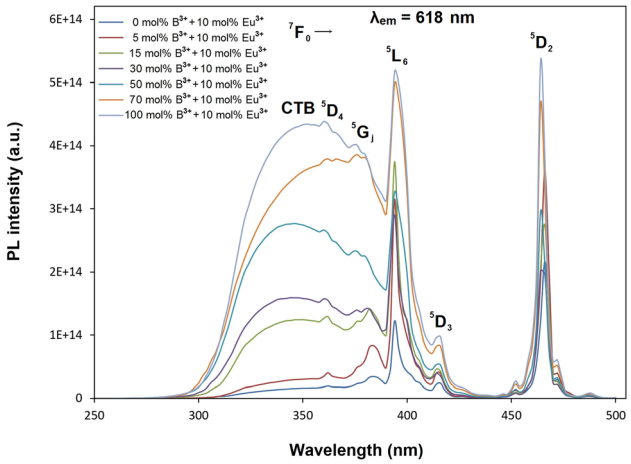

Fig. 4 PL excitation spectra and charge transfer bands of $BaTa_2O_6$:-xEu^{3+}, yB^{3+} phosphors corresponding to 618 nm emission.

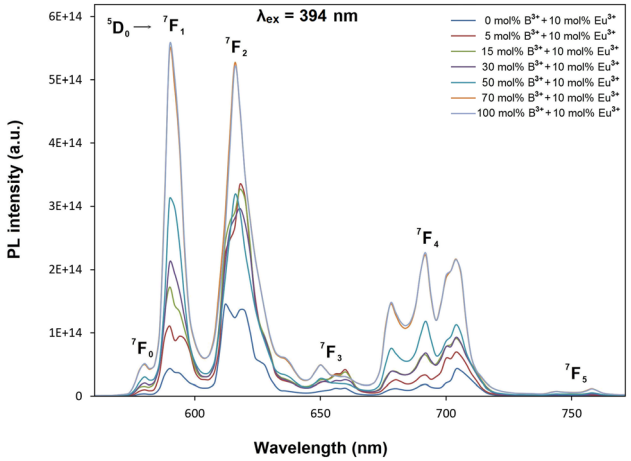

Fig. 5 PL emission spectra of $BaTa_2O_6$:xEu^{3+}, yB^{3+} phosphors with excitation of 394 nm.

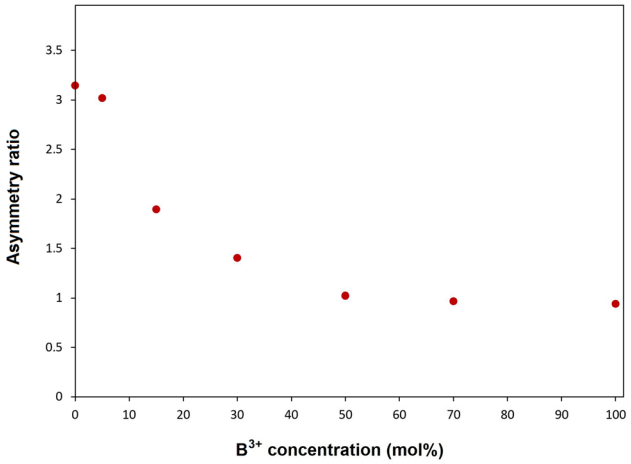

Fig. 6 Asymmetry ratio and boron concentration variation of $BaTa_2$-O_6:xEu^{3+}, yB^{3+} phosphors.

0 to 100 mol% B^{3+} for the magnetic dipole transition ($^5D_0 \rightarrow {}^7F_1$) and the electric dipole transition ($^5D_0 \rightarrow {}^7F_2$), respectively. In TTB structure, the pentagonal (A) sites are non-centrosymmetric and associated with the $^5D_0 \rightarrow {}^7F_2$ transition, where Eu^{3+} ions are sensitive to the crystal field. The square (B) sites are centrosymmetric and related to the $^5D_0 \rightarrow {}^7F_1$ transition in which the behavior of Eu^{3+} ions will not be affected by the crystal field.[33] The Eu^{3+} ions inserted to TTB-host are more likely to occupy A sites (15 CN) rather than B sites (12 CN). The improving magnetic dipole transition indicated that the increased presence of boron increases the activation of Eu^{3+} ions in the B sites. On the other hand, based on the increase in $^5D_0 \rightarrow {}^7F_1$ transition, a correlation between grain elongation and B site occupancy is noticeable. The magnetic dipole transitions of lanthanide ions are multiple transitions with strong magnetic dipole character and emission wavelengths throughout the near-infrared, visible, and ultraviolet (UV) spectral range, however, most of these transitions typically involve highly excited states that are rapidly decayed by non-radiative pathways such as multiphonon relaxation process.[35] Shan *et al.*[10] highlighted that prism and rod nanocrystals with the same surface area (SA)/volume (vol) ratios can exhibit different lattice energies and multiphonon relaxation processes. Furthermore, the phosphor with low luminescence generally has a larger surface-to-volume (SA/vol) ratio and a higher quenching defect fraction than the phosphor with good luminescence. The low phonon energy modes are cut off at smaller particle sizes due to the phonon confinement effect significantly reducing the energy transfer and luminescence between a donor and an acceptor.[36–38] Consequently, based on the occupancy of B site, the magnetic dipole character supports the multiphonon relaxation process, and it is also likely that the elongated grain shape with increasing grain size of the phosphor promotes the multiphonon relaxation process due to the difference in phonon energy.

Judd–Ofelt (JO) theory explains the intensity of electron transitions in 4f shell of rare-earth ions using three parameters and describes their spectral properties.[39,40] The JO intensity parameters Ω_J ($J = 2, 4, 6$) from the emission spectrum for Eu^{3+} can be determined by eqn (1):

$$\Omega_J = \frac{S_{MD}(V_1{}^3)}{e^2(V_J{}^3)} \frac{9n^3}{n(n^2+2)^2} \frac{\int I_1(V_1)}{|\langle J\|U^J\|J'\rangle|^2 \int I_J(V_J)} \quad (1)$$

where V is the transition frequency, I_1 and I_J for $^5D_0 \rightarrow {}^7F_1$ and $^5D_0 \rightarrow {}^7F_J$ transitions are the integrated intensities, respectively, $S_{MD} = 9.6 \times 10^{-42}$ (esu^2 cm^2) is the magnetic dipole line strength, n is the refractive index, $e = 4.803 \times 10^{-10}$ (esu) is the elementary charge, J and J' for the initial state and final state are the total angular momentum, respectively, $|\langle J\|U^J\|J\rangle|^2$ is the symbol of double reduced matrix elements for unit tensor operators. For all electric dipole (ED) transitions originating from the $^5D_0$ level, the reduced matrix elements are zero except for the $^5D_0 \rightarrow {}^7F_2$ ($U^2 = 0.0032$), $^5D_0 \rightarrow {}^7F_4$ ($U^4 = 0.0023$) and $^5D_0 \rightarrow {}^7F_6$ ($U^6 = 0.0002$) transitions. The $^5D_0 \rightarrow {}^7F_J$ ($J = 1, 2, 4, 6$) transitions are used for the determination of the radiative transition probabilities while $^5D_0 \rightarrow {}^7F_J$ ($J = 0, 3,$

5) transitions are prohibited, and are not included JO calculation. The $^5D_0 \rightarrow {}^7F_6$ transition related to Ω_6 parameter was not included in the calculation because it could not be detected by PL in the infrared region. However, the effect of this transition on the calculation is negligible, which has been reported in some studies.[18,29] The spontaneous transition probability (A) is related to its dipole strength which can be expressed as eqn (2):

$$A(J,J') = \frac{64\pi^4 V^3}{3h(2J+1)}[\mathcal{X}_{ED}S_{ED} + \mathcal{X}_{MD}S_{MD}] \quad (2)$$

where S_{ED} (electric dipole) and S_{MD} (magnetic dipole) are line strengths (in esu^2 cm^2), and h is Planck constant. The electric dipole line strengths (S_{ED}) from the JO parameters can be calculated by eqn (3):

$$S_{ED}(J,J') = e^2 \sum_{J=2,4,6} \Omega_J \cdot \left|\langle J\| U^J \|J'\rangle\right|^2 \quad (3)$$

The $\mathcal{X}_{ED}$ and $\mathcal{X}_{MD}$ are the local field corrections for the ED and MD transitions which can be found by eqn (4) and (5) respectively:

$$\mathcal{X}_{ED} = \frac{n(n^2+2)^2}{9} \quad (4)$$

$$\mathcal{X}_{MD} = n^3 \quad (5)$$

where n is the refractive index of $BaTa_2O_6$ which was taken as 1.891 from ref. 29 and 41 The Judd–Ofelt intensity parameters (Ω_2, Ω_4) are given in Table 2. The parameter Ω_2, which is closely related to the hypersensitive electric dipole transition ($^5D_0 \rightarrow {}^7F_2$), indicates the covalency of the Eu–O bond character and the environmental changes of the Eu^{3+} ion. The parameter Ω_4 is related to the electron density of the surrounding ligands, where an increase in the Ω_4 parameter shows a decreased electron density.[18,42] In Table 2, the Ω_2 parameter decreased from 5.299 to 1.506 $\times 10^{-20}$ cm^2, and the Ω_4 parameter decreased from 3.794 and 1.541 $\times 10^{-20}$ cm^2, with increasing B^{3+} concentration, respectively. The decreasing trend in the Ω_2 parameter showed weak covalent or strong ionic character of the Eu–O bond and high local symmetry of the Eu^{3+} sites, while the decrease in Ω_4 parameter indicated an increase in the electron density of the surrounding ligands. Moreover, the decreased Ω_4 parameter may be attributed to the increased charge transfer in the host which may be attributed to the reduction of Eu^{3+} to Eu^{2+} and a decrease in the electric dipole intensity. The branching ratio (β) of the Judd–Ofelt theory can be obtained from the radiated transition probability ($A(J,J')$) and the total radiated transition probability ($\Sigma A(J,J')$) using eqn (6), the results are given in Table 2:

$$\beta(\%) = \frac{A(J,J')}{\sum A(J,J')} \times 100\% \quad (6)$$

The branching ratio of the phosphors for the $^5D_0 \rightarrow {}^7F_2$ transition decreased due to the increasing magnetic dipole character. The β ratio of electric and magnetic transitions from 0 to 100 mol% B^{3+} changed to 60.98–39.65% and 17.79–40.62%, respectively.

Fig. 7 shows the decay curves of $^5D_0 \rightarrow {}^7F_2$ transition (618 nm) with excitation of 394 nm, for Eu^{3+}, B^{3+} co-doped phosphors. The two exponential decay curves can be defined using eqn (7):

Table 2 J–O parameters (Ω_2, Ω_4), radiative transition and total transition probabilities ($A(J,J')$, (A_r)), and branching ratios (β), of $BaTa_2O_6$:xEu^{3+}, yB^{3+} (x = 10 mol%, y = 0, 5, 15, 30, 50, 70, and 100 mol%) phosphors

B^{3+} conc. (mol%)	Eu^{3+} transitions	Ω_2 (10^{-20} cm^2)	Ω_4 (10^{-20} cm^2)	$A(J,J')$ (s^{-1})	A_r (s^{-1})	β (%)
0	$^5D_0 \rightarrow {}^7F_1$	5.299	3.794	99.008	556.462	17.79
	$^5D_0 \rightarrow {}^7F_2$			339.338		60.98
	$^5D_0 \rightarrow {}^7F_4$			118.115		21.23
5	$^5D_0 \rightarrow {}^7F_1$	4.878	2.417	99.092	486.692	20.36
	$^5D_0 \rightarrow {}^7F_2$			312.352		64.18
	$^5D_0 \rightarrow {}^7F_4$			75.249		15.46
15	$^5D_0 \rightarrow {}^7F_1$	3.063	2.014	99.011	357.839	27.67
	$^5D_0 \rightarrow {}^7F_2$			196.130		54.81
	$^5D_0 \rightarrow {}^7F_4$			62.697		17.52
30	$^5D_0 \rightarrow {}^7F_1$	2.240	1.659	98.843	293.924	33.63
	$^5D_0 \rightarrow {}^7F_2$			143.416		48.79
	$^5D_0 \rightarrow {}^7F_4$			51.665		17.58
50	$^5D_0 \rightarrow {}^7F_1$	1.645	1.437	98.744	248.823	39.68
	$^5D_0 \rightarrow {}^7F_2$			105.324		42.33
	$^5D_0 \rightarrow {}^7F_4$			44.755		17.99
70	$^5D_0 \rightarrow {}^7F_1$	1.546	1.542	98.846	245.835	40.21
	$^5D_0 \rightarrow {}^7F_2$			98.978		40.26
	$^5D_0 \rightarrow {}^7F_4$			48.012		19.53
100	$^5D_0 \rightarrow {}^7F_1$	1.506	1.541	98.817	243.259	40.62
	$^5D_0 \rightarrow {}^7F_2$			96.461		39.65
	$^5D_0 \rightarrow {}^7F_4$			47.981		19.73

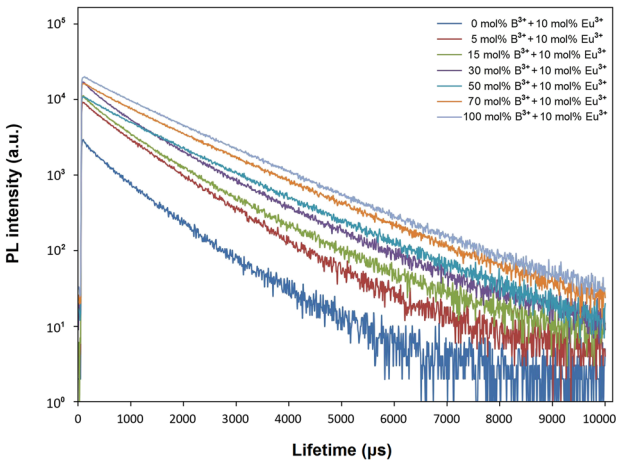

Fig. 7 Decay curves of $BaTa_2O_6$:xEu^{3+}, yB^{3+} phosphors with the emission of 618 nm and excitation of 394 nm.

$$I_t = I_0 + I_1 \exp\frac{-t}{\tau_1} + I_2 \exp\frac{-t}{\tau_2} \quad (7)$$

where I_t is PL intensity, t is the time after excitation, I_0 is the background, I_1 and I_2 are luminescence intensities corresponding to τ_1 (long) and τ_2 (short) lifetimes, respectively. Accordingly, the average or observed lifetime (τ) can be found by eqn (8):[41–45]

$$\tau = \frac{I_1\tau_1^2 + I_2\tau_2^2}{I_1\tau_1 + I_2\tau_2} \quad (8)$$

The variation of the bi-exponential decays depending on B^{3+} concentration is given in Table 3. The observed lifetimes increased from 0.934 to 1.362 μs in the range of 0–100 mol% B^{3+}, respectively. Based on the phonon energy of RE ions for the same host, a relatively longer PL lifetime is attributed to a more symmetrical site as the f–f transition becomes more forbidden,[46] where the decrease in asymmetry ratio or increase in local environmental symmetry of Eu^{3+} ions supports the decay results. In Table 3, the long lifetime (τ_1) and short lifetime (τ_2) with increased B^{3+} changed from 1.109 and 0.436 μs to 1.445 and 0.654 μs, respectively. The long lifetime (τ_1) is associated with RE^{3+} ions on the inside of the particle/isolated centers, and the short lifetime (τ_2) is related to RE^{3+} ions close to the surface and/or on the surface of the particle.[45,47] Besides, the long lifetime and the short lifetime are associated with high symmetry and low symmetry of Eu^{3+} ions, respectively.[46] The variation of the long ($\tau_1 \times I_1$) components and short ($\tau_2 \times I_2$) components depending on B^{3+} concentration is displayed in Fig. 8. The increase in the long and short components shows that the presence of boron increases the activation of Eu^{3+} luminescence centers in both particle core/isolated centers and on the particle surface. However, the increase in $\tau_1 \times I_1$ trend is higher than the $\tau_2 \times I_2$, indicating that the activation of Eu^{3+} centers within the particle is increased more than Eu^{3+} luminescence centers at or near the particle surface. Moreover, the increase in the $\tau_1 \times I_1$ trend supports the more symmetrical or magnetic dipole character of Eu^{3+} sites and the occupation of Eu^{3+} ions in B-centrosymmetric sites.

Table 3 Long (τ_1) and short (τ_2) lifetimes, long (I_1) and short (I_2) luminescence intensities, average (observed) lifetimes (τ) and chi-square (x^2) values for $BaTa_2O_6$:xEu^{3+}, yB^{3+} (x = 10 mol%, y = 0, 5, 15, 30, 50, 70, and 100 mol%) phosphors

B^{3+} conc. (mol%)	τ_1 (ms)	I_1	τ_2 (ms)	I_2	τ (ms)	x^2
0	1.109	2008	0.436	1801	0.934	1.123
5	1.049	5415	0.537	3837	0.913	1.104
15	1.227	5041	0.537	5828	0.995	1.232
30	1.250	8459	0.487	8344	1.038	1.249
50	1.366	10 280	0.439	7051	1.199	1.269
70	1.433	12 365	0.617	3821	1.337	1.073
100	1.445	15 783	0.654	4055	1.362	0.981

The quantum efficiency (η_{QE}) of the phosphors can be found from the ratio of the average (observed) lifetime (τ) to the radiative lifetime (τ_r) by eqn (9):

$$\eta_{QE} = \frac{\frac{1}{A_r + A_{nr}}}{\frac{1}{A_r}} = \frac{\tau}{\tau_r} \quad (9)$$

where the radiative and nonradiative transitions of $^5D_0$ level are A_r and A_{nr}, respectively. The radiative lifetimes (τ_r) and quantum efficiencies (η_{QE}) are tabulated in Table 4. The values of the η_{QE}% from 0 to 100 mol% B^{3+} varied to 51.95% and 33.14%, respectively, which corresponds to a decrease of approximately 36%, which may be attributed to the multiphonon relaxation process associated with the improving magnetic dipole character. Moreover, the energy transfer possibility between Eu^{3+}–Eu^{3+} ions can be predicted by eqn (10):[41]

$$\eta_{Eu\rightarrow Eu} = 1 - \frac{\tau}{\tau_0} \quad (10)$$

where τ_0 is the observed lifetime for low concentration. Table 4 summarizes the energy transfer probabilities decreased by approximately 46%, in which the increase in B^{3+} concentration caused the local environment of Eu^{3+} to become more

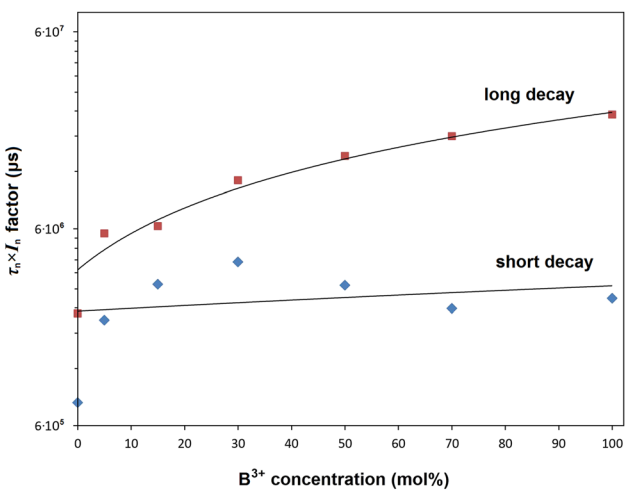

Fig. 8 Variation of product curves for the long ($\tau_1 \times I_1$) and short ($\tau_2 \times I_2$) components depending on the boron concentration.

Table 4 Radiative lifetimes (τ_r), observed lifetimes (τ), quantum efficiencies (η_{QE}) and energy transfer possibilities ($\eta_{Eu\rightarrow Eu}$) of $BaTa_2O_6$:-xEu^{3+}, yB^{3+} (x = 10 mol%, y = 0, 5, 15, 30, 50, 70, and 100 mol%) phosphors

B^{3+} conc. (mol%)	τ_r (ms)	τ (ms)	η_{QE} (%)	$\eta_{Eu\rightarrow Eu}$ (%)
0	1.797	0.934	51.95	0.00
5	2.055	0.913	44.43	2.23
15	2.795	0.995	35.61	−6.60
30	3.402	1.038	30.51	−11.17
50	4.019	1.199	29.83	−28.43
70	4.068	1.337	32.86	−43.19
100	4.111	1.362	33.14	−45.92

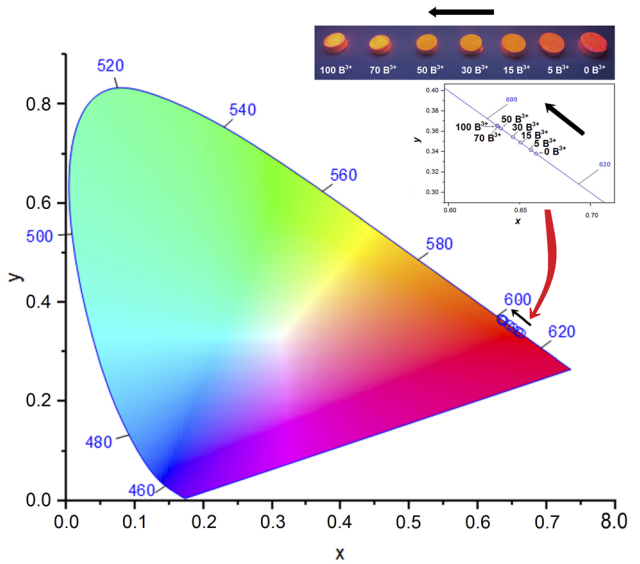

Fig. 9 CIE coordinates (x, y) and UV lamp photos at 365 nm of $BaTa_2O_6$:xEu^{3+}, yB^{3+} phosphors.

symmetrical and the energy transfer process to become more inhibiting.

Fig. 9 displays the chromaticity coordinates of $BaTa_2O_6$:-xEu^{3+}, yB^{3+} phosphors in the CIE diagram, illustrating how they vary depending on the concentration of Eu^{3+}. CIE coordinates (x, y) of the phosphors from 0 to 100 mol% B^{3+} changed to (0.6616, 0.3382) and (0.6339, 0.3657), respectively. The phosphor's emission shows a progression from red to orange as B^{3+} concentration increases. Thus, by augmenting the B^{3+} concentration in the CIE diagram, the emission of Eu^{3+} can be adjusted from the red region to the orange region. The UV lamp photographs of the phosphors under 365 nm are given in Fig. 9, in the inset figure. The UV lamp photo of the undoped boron sample has a red appearance, showing a transition towards an orange appearance with increasing B^{3+} concentration.

4. Conclusion

In the study, the effect of the grain size and grain shape on the spectral properties was investigated by using $BaTa_2O_6$:xEu^{3+}, yB^{3+} (x = 10 mol%, y = 0, 5, 15, 30, 50, 70, 100 mol%) co-doped phosphor ceramics. XRD results showed a single-phase structure up to 100 mol%, while the increase in B^{3+} concentration led to an improvement in crystallinity and an increase in reflections (001) and (002) associated with elongation in the z-direction. SEM examinations revealed the elongation and growth in grains with increasing B^{3+} concentration. The increase in PL emission was associated with improved crystallinity and grain growth or decreasing SA/vol ratio, while the increased magnetic dipole character of phosphor was attributed to centrosymmetric B-site occupation and grain elongation. The decrease in the Ω_2 and Ω_4 parameters indicated the high local symmetry of the Eu^{3+} sites and increased charge transfer in the host, respectively. The increased B^{3+} presence led to an increase in the observed lifetime, which is attributed to a more symmetrical site as the f–f transition becomes more forbidden. The increase in the long and short components showed the activation of Eu^{3+} centers within the grains and at/near the grain surfaces increased, in addition, the relatively high increase in long components supported the increased site symmetry and magnetic dipole character of Eu^{3+} ions. The decrease in quantum efficiency and energy transfer efficiency was 36% and 46% from 0 to 100 mol% B^{3+}, respectively. The decrease in quantum efficiency and energy transfer efficiency was associated with the increased multiphonon relaxation process resulting from the magnetic dipole transition. The variation of luminescence properties concerning grain morphology also demonstrates that they can be adjusted by controlling the reaction conditions.

Conflicts of interest

There are no conflicts to declare.

References

1 X. Liu, L. Li, H. M. Noh, J. H. Jeong, K. Jang and D. S. Shin, Controllable synthesis of uniform $CaMoO_4$:Eu^{3+}, M$^+$ (M = Li, Na, K) microspheres and optimum luminescence properties, *RSC Adv.*, 2015, **5**, 9441.
2 G. Jyothi, L. S. Kumaria and K. G. Gopchandran, Site selective substitution and its influence on photoluminescence properties of $Sr_{0.8}Li_{0.2}Ti_{0.8}Nb_{0.2}O_3$:Eu^{3+} phosphors, *RSC Adv.*, 2017, **7**, 28438.
3 Y. Hua, T. Wang, J. S. Yu, W. Ran and L. Li, Modulating A site compositions of europium(III)-doped double-perovskite niobate phosphors, *Inorg. Chem. Front.*, 2022, **9**, 6211–6224.
4 M. Chowdhury and S. K. Sharma, Spectroscopic behavior of Eu^{3+} in SnO_2 for tunable red emission in solid state lighting devices, *RSC Adv.*, 2015, **5**, 51102.
5 C. Y. Peng, B. Wang, L. F. Yuan, K. G. Hu, G. Chen, H. Y. Wu, Y. H. Hu and Y. H. Jin, Six- and five-coordinated Cr^{3+} in Ga_2GeO_5 invokes tunable broadband near-infrared emission toward night-vision applications, *Rare Met.*, 2023, **42**, 3787–3796.
6 C. Peng, L. Yuan, G. Chen, H. Wu and Y. Jin, Thermally stable broadband near-infrared emitting pyrochlore oxide phosphors codoped with Cr^{3+} and Yb^{3+} ions, *Ceram. Int.*, 2024, **50**, 7059–7066.

7 M. İlhan, M. K. Ekmekçi and İ. Ç. Keskin, Judd–Ofelt parameters and X-ray irradiation results of MNb2O6:Eu3+ (M = Sr, Cd, Ni) phosphors synthesized via a molten salt method, *RSC Adv.*, 2021, **11**, 10451–10462.

8 M. İlhan and İ. Ç. Keskin, Analysis of Judd–Ofelt parameters and radioluminescence results of $SrNb_2O_6$:Dy^{3+} phosphors synthesized via molten salt method, *Phys. Chem. Chem. Phys.*, 2020, **22**, 19769.

9 Y. Kim and S. Kang, Effect of particle size on photoluminescence emission intensity in ZnO, *Acta Mater.*, 2011, **59**, 3024–3031.

10 J. Shan, M. Uddi, R. Wei, N. Yao and Y. Ju, The hidden effects of particle shape and criteria for evaluating the upconversion luminescence of the lanthanide doped nanophosphors, *J. Phys. Chem. C*, 2010, **114**, 2452–2461.

11 J. Y. Park, H. C. Jung, G. S. R. Raju, B. K. Moon, J. H. Jeong, S. M. Son and J. H. Kim, Sintering temperature effect on structural and luminescence properties of 10 mol% Y substituted $Gd_3Al_5O_{12}$:Ce phosphors, *Opt. Mater.*, 2009, **32**, 293–296.

12 G. S. R. Raju and S. Buddhudu, Emission analysis of Tb^{3+}:$MgLaLiSi_2O_7$ powder phosphor, *Mater. Lett.*, 2008, **62**, 1259–1262.

13 G. Wakefield, E. Holland, P. J. Dobson and J. L. Hutchison, Luminescence properties of nanocrystalline Y_2O_3:Eu, *Adv. Mater.*, 2001, **13**, 1557.

14 K. Y. Jung, C. H. Lee and Y. C. Kang, Effect of surface area and crystallite size on luminescent intensity of Y_2O_3:Eu phosphor prepared by spray pyrolysis, *Mater. Lett.*, 2005, **59**, 2451–2456.

15 M. İlhan, M. K. Ekmekçi, A. Mergen and C. Yaman, Photoluminescence characterization and heat treatment effect on luminescence behavior of $BaTa_2O_6$:Dy^{3+} phosphor, *Int. J. Appl. Ceram. Technol.*, 2017, **14**, 1134–1143.

16 B. Demir, D. Derince, T. Dayioglu, L. Koroglu, E. Karacaoglu, V. Uz and E. Ayas, Effects of doping content and crystallite size on luminescence properties of Eu^{3+} doped fluorapatites obtained from natural waste, *Ceram. Int.*, 2021, **47**, 34657–34666.

17 W. N. Wang, W. Widiyastuti, T. Ogi, I. W. Lenggoro and K. Okuyama, Correlations between crystallite/particle size and photoluminescence properties of submicrometer phosphors, *Chem. Mater.*, 2007, **19**, 1723–1730.

18 M. İlhan and L. F. Güleryüz, Boron doping effect on the structural, spectral properties and charge transfer mechanism of orthorhombic tungsten bronze β-$SrTa_2O_6$:Eu^{3+} phosphor, *RSC Adv.*, 2023, **13**, 12375.

19 M. İlhan, M. K. Ekmekçi and L. F. Güleryüz, Effect of boron incorporation on the structural, morphological, and spectral properties of $CdNb_2O_6$:Dy^{3+} phosphor synthesized by molten salt process, *Mater. Sci. Eng., B*, 2023, **298**, 116858.

20 Y. Huang, Q. Feng, Y. Yang and H. J. Seo, A study of luminescence properties in the boron-doped lead tungstate, *Phys. Lett. A*, 2005, **336**, 490–497.

21 H. He, Y. Wang and Y. Zou, Room temperature photoluminescence property of boron-doped sol–gel silica, *Mater. Res. Bull.*, 2004, **39**, 747–753.

22 Y. C. Kang, H. S. Roh and S. B. Park, Improvement of brightness of Gd_2O_3:Eu phosphor particles using boric acid flux in the spray pyrolysis, *Jpn. J. Appl. Phys.*, 2000, **39**, L31–L33.

23 K. S. Lau, Z. Hassan, W. F. Lim and H. J. Quah, Synthesis and luminescence enhancement of red-emitting $Ca_3Y(AlO)_3(BO_3)_4$:Eu^{3+} phosphors via La^{3+} Co-doping prepared by microwave solution combustion synthesis, *Mater. Chem. Phys.*, 2022, **292**, 126649.

24 M. Szkoda, A. L. Oleksiak and K. Siuzdak, Optimization of boron-doping process of titania nanotubes via electrochemical method toward enhanced photoactivity, *J. Solid State Electrochem.*, 2016, **20**, 1765–1774.

25 A. Nakamura, N. Nambu and H. Saitoh, Effect of boron concentration in Y_2O_3:(Eu,B) phosphor on luminescence property, *Sci. Technol. Adv. Mater.*, 2005, **6**, 210–214.

26 D. Chen, D. Yang, Q. Wang and Z. Jiang, Effects of boron doping on photocatalytic activity and microstructure of titanium dioxide nanoparticles, *Ind. Eng. Chem. Res.*, 2006, **45**, 4110–4116.

27 K. Dhanalakshmi and A. J. Reddy, Effect of flux boric acid (H_3BO_3) on yttrium silicate Y_2SiO_5:Dy^{3+} (9 mol%) nanophosphors its characterization and luminescence studies, *Sens. Lett.*, 2019, **17**, 898–904.

28 A. Dulda, D. S. Jo, W. J. Park, T. Masaki and D. H. Yoon, Photoluminescence and morphology of flux grown BAM phosphor using a novel synthesis method, *J. Ceram. Process. Res.*, 2009, **10**, 811–816.

29 M. İlhan, M. İ. Katı, İ. Ç. Keskin and L. F. Güleryüz, Evaluation of structural and spectroscopic results of tetragonal tungsten bronze MTa_2O_6: Eu^{3+} (M = Sr, Ba, Pb) phosphors and comparison on the basis of Judd–Ofelt parameters, *J. Alloys Compd.*, 2022, **901**, 163626.

30 İ. Ç. Keskin and M. İlhan, Thermoluminescence kinetic parameters and radioluminescence of RE^{3+} (RE = Pr, Sm, Tb, Ho, Er)-doped barium tantalate phosphors, *J. Electron. Mater.*, 2023, **52**, 5614–5630.

31 M. İlhan, A. Mergen and C. Yaman, Removal of iron from $BaTa_2O_6$ ceramic powder produced by high energy milling, *Ceram. Int.*, 2013, **39**, 5741–5750.

32 M. İlhan, A. Mergen and C. Yaman, Mechanochemical synthesis and characterisation of $BaTa_2O_6$ ceramic powders, *Ceram. Int.*, 2011, **37**, 1507–1514.

33 G. Li, L. Cheng, F. Liao, S. Tian, X. Jing and J. Lin, Luminescent and structural properties of the series $Ba_{6-x}Eu_xTi_{2+x}Ta_{8-x}O_{30}$ and $Ba_{4-y}K_yEu_2Ti_{4-y}Ta_{6+y}O_{30}$, *J. Solid State Chem.*, 2004, **177**, 875–882.

34 J. Hou, P. Chen, G. Zhang, Y. Fang, W. Jiang, F. Huang and Z. Ma, Synthesis, structure and photoluminescence properties of tetragonal tungsten bronze-type Eu^{3+}-doped $K_2LaNb_5O_{15}$ niobate phosphor, *J. Lumin.*, 2014, **146**, 97–101.

35 F. T. Rabouw, P. T. Prins and D. J. Norris, Europium-doped $NaYF_4$ nanocrystals as probes for the electric and magnetic local density of optical states throughout the visible spectral range, *Nano Lett.*, 2016, **16**, 7254–7260.

36 H. X. Mai, Y. W. Zhang, L. D. Sun and C. H. Yan, Highly efficient multicolor up-conversion emissions and their

mechanisms of monodisperse NaYF4:Yb,Er core and core/shell-structured nanocrystals, *J. Phys. Chem. C*, 2007, **111**, 13721–13729.

37 G. K. Liu, H. Z. Zhuang and X. Y. Chen, Restricted phonon relaxation and anomalous thermalization of rare earth ions in nanocrystals, *Nano Lett.*, 2002, **2**, 535–539.

38 X. Y. Chen, H. Z. Zhuang, G. K. Liu, S. Li and R. S. Niedbala, Confinement on energy transfer between luminescent centers in nanocrystals, *J. Appl. Phys.*, 2003, **94**, 5559–5565.

39 B. R. Judd, Optical absorption intensities of rare-earth ions, *Phys. Rev.*, 1962, **127**, 750.

40 G. S. Ofelt, Intensities of crystal spectra of rare-earth ions, *J. Chem. Phys.*, 1962, **37**, 511.

41 M. İlhan, İ. Ç. Keskin, L. F. Güleryüz and M. İ. Katı, A comparison of spectroscopic properties of Dy^{3+}-doped tetragonal tungsten bronze MTa_2O_6 (M = Sr, Ba, Pb) phosphors based on Judd–Ofelt parameters, *J. Mater. Sci.: Mater. Electron.*, 2022, **33**, 16606–16620.

42 R. Saraf, C. Shivakumara, S. Behera, H. Nagabhushana and N. Dhananjaya, Photoluminescence, photocatalysis and Judd– Ofelt analysis of Eu^{3+}-activated layered BiOCl phosphors, *RSC Adv.*, 2015, **5**, 4109.

43 N. Yaiphaba, R. S. Ningthoujam, N. S. Singh, R. K. Vatsa, N. R. Singh, S. Dhara, N. L. Misra and R. Tewari, Luminescence, lifetime, and quantum yield studies of redispersible Eu^{3+}-doped $GdPO_4$ crystalline nanoneedles: Core-shell and concentration effects, *J. Appl. Phys.*, 2010, **107**, 034301.

44 N. S. Singh, R. S. Ningthoujam, N. Yaiphaba, S. D. Singh and R. K. Vatsa, Luminescence, lifetime and quantum yield studies of YVO_4:Ln^{3+} (Ln^{3+} = Dy^{3+}, Eu^{3+}) nanoparticles: Concentration and annealing effects, *Chem. Phys. Lett.*, 2009, **480**, 237–242.

45 A. K. Parchur and R. S. Ningthoujam, Behaviour of electric and magnetic dipole transitions of Eu^{3+}, $^5D0 \rightarrow {}^7F_0$ and Eu–O charge transfer band in Li^+ co-doped YPO_4:Eu^{3+}, *RSC Adv.*, 2012, **2**, 10859–10868.

46 S. K. Gupta, J. P. Zuniga, M. Abdou, P. S. Ghoshc and Y. Mao, Optical properties of undoped, Eu^{3+} doped and Li^+ co-doped $Y_2Hf_2O_7$ nanoparticles and polymer nanocomposite films, *Inorg. Chem. Front.*, 2020, **7**, 505.

47 V. Sudarsan, F. C. J. M. van Veggel, R. A. Herring and M. Raudsepp, Surface Eu^{3+} ions are different than ''bulk'' Eu^{3+} ions in crystalline doped LaF_3 nanoparticles, *J. Mater. Chem.*, 2005, **15**, 1332.